

Hinode/EIS measurements of active region magnetic fields

E. Landi

Department of Climate and Space Sciences and Engineering, University of Michigan

R. Hutton

Institute of Modern Physics, Fudan University, Shanghai 200433, People's Republic of China

T. Brage

Department of Physics, Lund University, Box 118, SE-22100 Lund, Sweden

W. Li

Department of Physics, Lund University, Box 118, SE-22100 Lund, Sweden

Department of Materials Science and Applied Mathematics, Malmö University, SE-20506, Malmö, Sweden

ABSTRACT

The present work illustrates the potential of a new diagnostic technique that allows the measurement of the coronal magnetic field strength in solar active regions utilizing a handful of bright Fe X and Fe XI lines commonly observed by the Hinode/EIS high-resolution spectrometer. The importance of this new diagnostic technique lies in two basic facts: 1) the coronal magnetic field is probably the most important quantity in coronal physics, as it is at the heart of the processes regulating Space Weather and the properties of the solar corona, and 2) this technique can be applied to the existing EIS archive spanning from 2007 to 2020, including more than one full solar cycle and covering a large number of active regions, flares, and even coronal mass ejections. This new diagnostic technique opens the door to a whole new field of studies, complementing the magnetic field measurements from the upcoming DKIST and UCoMP ground based observatories, and extending our reach to active regions observed on the disk and until now only sampled by radio measurements. In this work we present a few examples of the application of this technique to EIS observations taken at different times during the EIS mission, discuss its current limitations and the steps to improve its accuracy. We also present a list of EIS observing sequences

whose data include all the lines necessary for the application of this diagnostic technique, to help the solar community navigate the immense set of EIS data and to find observations suitable to measure the coronal magnetic field.

Subject headings: Sun: corona – Sun: magnetic field

1. Introduction

The magnetic field of the solar corona is one of the most critical parameters in solar physics, as it lies at the core of most manifestations of coronal physics and of the interactions between the Sun and its planetary system. In fact, the magnetic field confines and structures coronal plasmas at all temperature and spatial scales, from bright points (few tens of arcseconds in size), to coronal loops and active regions (arcminutes) and streamers (solar radii). Also, regions of open and closed magnetic fields have very different properties, with the former being the site of the acceleration of the fast solar wind and possibly of a part of the slow solar wind (Stakhiv *et al.* 2015, 2016). Several types of magnetic waves have been proposed as candidates to heat the solar coronal plasmas up to multimillion degrees temperatures, as well as to accelerate the solar wind along open magnetic field lines (e.g. Cranmer 2009, Gombosi *et al.* 2018 and references therein). Magnetic reconnection has been suggested as a viable alternative for coronal heating and wind acceleration (Cranmer 2009), and is thought to be the trigger of both flares and coronal mass ejections (Webb & Howard 2012 and references therein).

Despite its importance, the coronal magnetic field has proved elusive to infer directly, and very few measurements have been carried out. The photospheric magnetic field has been routinely measured by a number of space missions in the last few decades by instruments such as SoHO/MDI (Scherrer *et al.* 1995), Hinode/SOT (Suematsu *et al.* 2008) and SDO/HMI (Scherrer *et al.* 2012), and it is a fundamental component for local and global models of the solar atmosphere. Measurements of the coronal magnetic field are more difficult, because of the weakness of its signatures, and of the complexity of the measurements. Indirect measurements have been carried out studying coronal loop seismology (De Moortel *et al.* 2016) and magnetic field morphology has been empirically derived by active region plasma distribution. The only direct measurements so far have been obtained with radio observations, and spectropolarimetry of visible and near infrared (NIR) radiation, mostly with the Coronal Magnetometer and Polarimeter (CoMP, Tomczyk *et al.* 2008).

To improve on CoMP measurements, and to provide at the same time measurements both of the magnetic field and of coronal plasma properties, two new ground based instru-

ments are being built and are becoming operational in 2020: the Upgraded CoMP (UCoMP, Tomczyk *et al.* 2020, in preparation), and most importantly the Daniel K. Inohue Solar Telescope (DKIST). Both instruments will measure the coronal magnetic field through visible and NIR spectropolarimetry, with a vastly different field of view and resolution: while the DKIST observatory (which will comprise a host of different instruments) will provide high spatial resolution measurements over a small field of view, UCoMP will provide near-simultaneous lower resolution measurements over the entire solar corona.

However, ground based spectropolarimetric magnetic field measurements of the coronal magnetic fields suffer from a few fundamental limitations. First, they are affected by the day/night cycle and by atmospheric transmission and scattering, although such a limitation has been overcome by space-based instruments. Second, since they observe in the visible and NIR wavelength ranges, they can only carry out measurements at the limb using coronagraphs, as the photospheric brightness prevents any measurements of coronal emission to be carried out on the disk. Third, limb observations in the visible and NIR can only provide magnetic field orientation in the plane of the sky (through linear polarization – Stokes U and Q) and the magnetic field component along the line of sight (through circular polarization – Stokes V), so that the total magnitude of the magnetic field can not be reconstructed. Furthermore, the signal of Stokes V is weaker than the signal of Stokes U and Q, so that often only the magnetic field orientation in the plane of the sky can be measured.

The only measurements of coronal magnetic fields on the disk are done using radio measurements, sometimes in combination with Extreme Ultraviolet (EUV) observations. These measurements, however, are typically able to yield magnetic field strengths usually in excess of ≈ 200 G, and thus are most suitable for active regions. For example, Brosius *et al.* (2002) and Brosius & White (2006) combined EUV and radio observations of active regions on the disk to infer magnetic field strengths in the 580-1750 G range. White *et al.* (2002) measured the magnetic field of a flaring loop and found that it ranged from ≈ 800 G at the footpoints to 224 G at the top; similar values were found by Nindos *et al.* (2000) (870 G to 280 G). Still, radio measurements are able to provide the magnetic field at different heights within the same magnetic structure, but are not able to determine the actual height of the structure itself, thus leaving a significant uncertainty on the 3D orientation of the magnetic field vector.

Disk observations of the solar corona have been routinely carried out by imaging instruments and high resolution spectrometers observing in the X-ray, EUV and Ultraviolet (UV) wavelength ranges by a host of rocket flights and space missions (e.g. Del Zanna & Mason 2018 and references therein). These instruments constitute the backbone of our studies of the solar corona, as these wavelength ranges include a wealth of spectral lines and continuum

radiation that provide plasma diagnostic tools allowing us to measure fundamental plasma properties such as electron densities and temperatures, plasma motions and elemental composition (Phillips *et al.* 2008, Del Zanna & Mason 2018). However, the effects of coronal magnetic fields on the intensities, wavelengths and profiles of emission lines in the X-ray, EUV and UV ranges are too small to be detected, so that no diagnostic tool is available to measure the magnetic field directly from line intensities in these wavelength ranges.

Recently, Li *et al.* (2015, 2016) and Si *et al.* (2020a) reported on a peculiar atomic physics configuration which makes the wavefunction composition of a low-energy metastable atomic level of Fe X sensitive to the presence of an external magnetic field. This sensitivity would remain a curious feature of a single, metastable Fe X, if this level didn't happen to significantly contribute to the emission of one of the strongest lines in the Fe X spectrum in the solar corona at 257.26 Å. The properties of this metastable level cause the intensity of the line it emits to be directly and significantly affected by the local magnetic field strength; since this ion is usually formed in the corona, this property opens a window through which we can directly measure the magnetic field strength in the solar corona, which was first explored by Si *et al.* (2020b).

The 257.26 Å line has been routinely observed by the EIS spectrometer (Culhane *et al.* 2007) on board the Hinode satellite (Kosugi *et al.* 2007), along with many other Fe X lines for more than one solar cycle (2007 to mid-2020 at the time of writing). The vast data set accumulated by the EIS mission can be utilized to measure the coronal magnetic field strengths throughout the solar cycle. The first application of this line to determine magnetic fields in a Hinode/EIS active region has been described by Si *et al.* (2020b).

The goal of this paper is to refine and extend the diagnostic technique by making use of a few of the strongest Fe X and Fe XI lines routinely observed by the Hinode/EIS spectrometer from 2007 to 2020 to measure the magnetic field of the solar corona, present some examples, and discuss this diagnostic technique's strengths and limitations, as well as its synergies with the upcoming DKIST and UCoMP observatories. Future papers will apply this diagnostic technique to a number of different open problems in the solar corona. Section 2 introduces the diagnostic technique and its physical bases, Section 3 describes the Hinode/EIS observing sequences that can be used to apply the technique, as well as the actual observations we analyzed, and Section 4 presents the magnetic field measurements we obtained. Section 5 discusses the uncertainties in the present method, and Section 6 suggests future steps to improve on this technique.

2. Methodology

2.1. History of Magnetically Induced Transitions

The influence of magnetic fields on atomic energy levels has a history going back to Zeeman in 1896. The Zeeman effect is used in many areas to measure the strength of external magnetic fields. What is much less known is the influence of external magnetic fields on the lifetimes of long lived levels, through an introduction of a new decay channel – potentially resulting in new spectral features. The idea that a magnetic field could shorten the lifetime of a long lived level was investigated in the 1960s and was labelled *Zeeman quenching* by Feldman *et al.* (1967). The quenching was only considered through the shortening of, for example, the $1s2s2p\ ^4P_{5/2}$ lifetime in Li I and as an error source when trying to estimate the lifetimes in expected field-free space. The idea of a new or a change of an existing feature due to an external field did not seem to have any practical applications and the studies did not flourish. More recently, Beiersdorfer *et al.* (2003) used the Electron Beam Ion Trap (EBIT) at the Lawrence Livermore National Laboratory for the first observation of a spectral line induced by an external magnetic field – the $2p^53s\ ^3P_0-2p^6\ ^1S_0$ transition in Ne-like Argon. This transition is strictly forbidden (being a $J=0$ to $J=0$) in the absence of an external magnetic field (or nuclear spin). The induction of this transition requires a field of a few Tesla and was considered mainly of importance for understanding the atomic structure (as well as predicting nuclear properties in non-zero spin isotopes), not for applications to astrophysical plasmas: the required field and low density did not offer any possible observations.

Some years later a study was initiated by some of the present authors (TB, RH, WL) to find transitions induced by much lower magnetic field strengths. The basic atomic structure needed for the induction of a spectral line through an external magnetic field is two energy levels, relatively close in energy, where one has an allowed decay, and therefore short lifetime, while the other one should be at least metastable with a considerably longer lifetime. If the effect should be observable for small magnetic fields, the energy splitting between the levels has to be small, so the search focused on 'accidental' pseudo-degeneracy, induced by level crossing in the gross structure of ions, along an isoelectronic sequence. It represented a major breakthrough when the project focused on the interesting isoelectronic behavior of the $3s^23p^43d\ ^4D$ term in Cl-like ion, observed by isoelectronic studies and observations as reported in the NIST database (Kramida *et al.* 2019).

The 4D term has four energy levels of which the $^4D_{7/2}$ level is metastable and can only decay to the ground $J=3/2$ level of the $3s^23p^5\ ^2P$ term by a forbidden, magnetic quadrupole (M2), in the absence of an external field, since J must change by 2 units. However, the $^4D_{5/2}$ level has an allowed, electric dipole (E1) decay channel to the $^2P_{3/2}$ level (albeit spin-

changing), leading to a lifetime five orders of magnitude shorter. The ordering of these two levels changes along the sequence and as discussed by Li *et al.* (2015) the minimum energy separation between these two levels occurs for Fe X, leading to a pseudo-degeneracy. In this work it was shown for the first time that there was definitely a magnetic induced transition, MIT, from the $^4D_{7/2}$ level of Fe X, induced by the external magnetic field mixing of the two levels – the $J=7/2$ acquires some of the $J=5/2$ levels properties, including a decay channel to the ground term. It was also clear that this MIT was sensitive to fairly small magnetic fields. One problem discussed by Li *et al.* (2015) was the fact that the energy splitting of the two levels, which is crucial for the required sensitivity of the MIT to the low enough external magnetic field strengths, was not known accurately enough. In a following work by Li *et al.* (2016), the Shanghai high temperature superconducting EBIT with known magnetic field was used to obtain a value for the $^4D_{5/2}$ - $^4D_{7/2}$ fine structure energy. The energy obtained was 3.5 cm^{-1} , which agreed with the astrophysical estimate of $0 - 5 \text{ cm}^{-1}$, however with a large uncertainty (the astrophysical estimate do not offer any explicit guidance on uncertainty). Li *et al.* (2016) also showed that a line ratio of the $^4D_{7/2}$ and $^4D_{5/2}$ blended transitions with the transition from one of the other 4D levels could be used as a magnetic field diagnostic. Inspired by these initial efforts, Judge *et al.* (2016) used spectra of the solar corona from SkyLab to improve on the uncertainty of the $^4D_{5/2,7/2}$ fine structure energy and arrived at the result of $3.6 \pm 2.7 \text{ cm}^{-1}$. Recently this fine structure value was used in a determination of the magnetic field for an active region of the solar corona from spectral data from Hinode (Si *et al.* 2020b). Even more recently, Landi *et al.* (2020) improved on the measurement by Judge *et al.* (2016) using spectra from the SOHO/SUMER high resolution spectrometer, to obtain an energy separation of $2.29 \pm 0.50 \text{ cm}^{-1}$, which significantly lower the uncertainty (see Section 5); in the present work, we will be using this value.

2.2. Conceptual description of the MIT

The core of the method discussed in this paper is the concept of mixing of atomic states of the same parity but different J-values. The strength of the mixing depends strongly on the separation of the levels in energy and the magnetic field strength (both squared). All interactions between the electrons are diagonal in the total angular momentum quantum number J. Therefore two levels such as the $3s^23p^43d$ $^4D_{5/2}$ and $^4D_{7/2}$ in Cl-like ions cannot be mixed due to electron-electron interaction, even if the levels are basically energy degenerate. To induce this mixing and thereby the decay of the metastable level, we need to introduce interactions outside the electronic cloud, e.g. an externally applied magnetic field, which can mix levels with J differing by 0 or ± 1 . The other possibility for this mixing to occur, is through a nuclear spin, which changes the total angular momentum of the ion. In the cases

reported here, we only consider nuclei with zero spin.

It is important to note that the mixing of the $3s^23p^43d$ $^4D_{5/2}$ and $^4D_{7/2}$ and the resulting MIT in Cl-like Fe can be induced by unexpectedly small fields, of the order of a few hundred Gauss (or less). This is to be compared to the internal magnetic field of Fe X, caused by the orbiting electrons and their spins, which is of the order of many hundreds or even thousands of Tesla. As a metaphor, one could use that the external field only tickles the ion, but the accidental pseudo-degeneracy of two levels causes it to decay with a EUV-photon from the metastable state.

2.3. Measuring the magnetic field with the MIT

The most direct way to utilize the magnetically induced transition to measure the ambient magnetic field is to determine the MIT/M2 branching ratio from the observations. The first step is to disentangle the intensity of the two spectral lines at 257.26 Å in order to separate the E1 component from the MIT+M2 component. However, the energy separation between the $^4D_{7/2}$ and $^4D_{5/2}$ levels gives rise to a difference in the corresponding wavelengths of only ≈ 4 mÅ, which is by far too small to be resolved by either Hinode/EIS or any other high-resolution spectrometer built so far, and is also much smaller than the line broadening in the corona. Thus, the MIT+M2 fraction needs to be determined by indirect means.

In principle, any Fe X line intensity ratio involving the 257.26 Å is dependent on the magnetic field. However, since the metastable nature of the upper $^4D_{7/2}$ level causes all ratios involving this line to also be density sensitive, an independent measurement of the electron density needs to be available before determining the magnetic field.

Si *et al.* (2020b) proposed the use of two Fe X spectral lines to measure the magnetic field: 174.53 Å, 175.26 Å, in addition to the 257.26 Å. Their technique relied on comparing the measured 174.53/257.26 intensity ratio with theoretical estimates carried out at multiple values of the ambient magnetic field strength, B . The electron density was estimated using the 175.26/174.53 ratio, which has two advantages: first, it is the most density-sensitive ratio in the EUV Fe X spectrum; second, these two lines are strong features in the spectra. However, they are located in wavelength at the edge of the EIS passband, leading to their signal-to-noise ratio (SNR) being low in EIS observations. Therefore they are seldom included in the line selection to be telemetered down from the satellite. This is especially true when images of the magnetic field in active regions are sought, for which rebinning can be limited and thus, even if available, the 174.53 Å and 175.26 Å may have too low SNR. Thus, while the approach in itself is powerful, it can only be applied to a limited number of EIS

observations.

In this paper, we developed a different approach, which utilizes the brightest, and most commonly observed Fe X spectral line to obtain the same measurement: the 184.54 Å line. Furthermore, we utilized the CHIANTI database (V 9.0, Dere *et al.* 1997, 2019) to disentangle both the MIT and M2 line intensities from the observations, to determine their branching ratios and compare the results directly to the atomic physics calculations as a function of B .

The presence of a MIT contribution can be determined by measuring the intensity I_{MIT} of the 257.26 Å line in excess from the value predicted by CHIANTI neglecting its presence, as

$$I_{MIT} = I_{257} - I_{184} \times R(257/184) \quad (1)$$

where I_{257} and I_{184} are the measured intensities for the 257.26 Å and 184.54 Å lines, respectively, and $R(257/184)$ is the intensity ratio predicted by CHIANTI including both the E1 and M2 components, but not the MIT one. That is, Equation 1 measures the excess emission in the 257.26 Å that CHIANTI can not account for with only the M2 and E1 transitions.

The intensity I_{M2} of the M2 transition can be directly determined as

$$I_{M2} = I_{184} \times R(M2/184) \quad (2)$$

where $R(M2/184)$ is the ratio between the M2 component and the 184.54 Å line, also predicted by CHIANTI. The ratio I_{MIT}/I_{M2} can then be directly compared with the branching ratio predicted by Li *et al.* (2015), and shown in Figure 1.

There are two things to note. First, both the $R(257/184)$ and the $R(M2/184)$ are sensitive to the electron density n_e , the sensitivity being largest when $n_e > 10^9 \text{ cm}^{-3}$, typical of active regions. Thus, an independent estimate of the electron density is necessary for this ratio. Si *et al.* (2020b) chose the best line ratio to carry out the estimate, namely the 174.53/175.26 ratio. This ratio should be used whenever possible. However, since Hinode/EIS observations have low SNR for 174.53 Å and 175.26 Å lines, and often do not include them, it is often necessary to use another ratio.

The other Fe X lines in the EIS range are weaker, and while a few individual observations can include them, they can not be used for extensive application to magnetic field measurements, and thus it is necessary to resort to density sensitive ratios from other ions. These ions need to be formed close in temperature to Fe X, and need to provide line pairs with strong lines routinely observed and telemetered down by EIS. The best candidate is

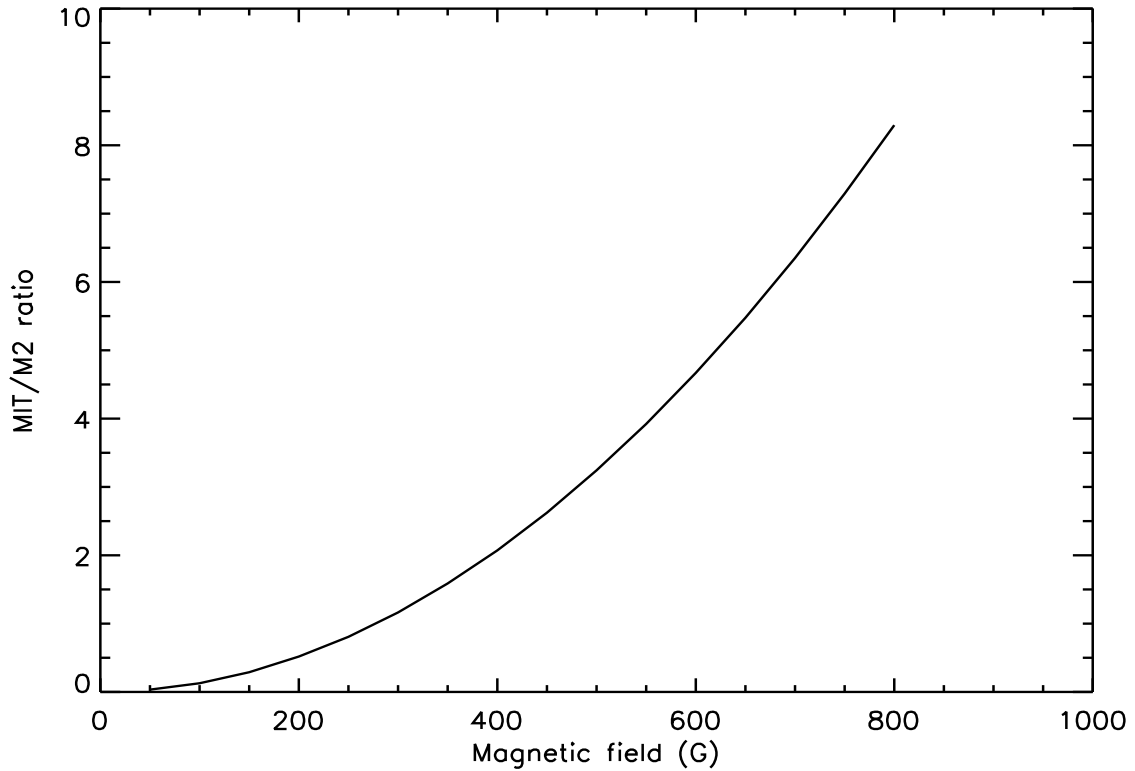


Fig. 1.— A_{MIT}/A_{M2} branching ratio as a function of magnetic field magnitude, in Gauss.

Fe XI 182.17/(188.22+188.30) line ratio. These Fe XI lines are strong, and extensively included in EIS observing sequences; the 188.2 doublet is only partially resolved by EIS, but its intensity can be easily measured either by a double Gaussian fit or simply by summing all the counts under the profile and subtracting the background. This doublet is sufficiently strong and isolated to allow for both options. These lines are stronger than those available for density diagnostics in the EIS line list for Fe IX – the other closest Fe ion – or for ions of other elements.

In principle, the Fe VIII 185.21/186.60 intensity ratio can also be used as density diagnostics to measure the magnetic field in cold, isolated loop structures when no other lines are present. Both these lines are bright and isolated, are often telemetered to the ground, and provide a sensitive density diagnostic line pair. However, care should be taken in checking that the intensity distribution of Fe VIII and Fe X is the same, to minimize errors and make sure that the emitting plasma is the same and the temperature difference between these two ions is not a problem. A similar caution needs to be taken when using the other line pairs

commonly included in EIS observing sequences: Fe XII 186.8/195.1 and Fe XIII 203.8/202.0: both ions are formed at a significantly higher temperature than Fe X. We discuss the uncertainties due to electron density determination in Section 5.

Another critical point to note is that the 257.26 Å line is the only strong Fe X line in the long wavelength (LW) detector, while all others are observed in the short wavelength (SW) one. This makes the relative calibration of the two detectors a critical factor in the measurement of coronal magnetic fields. The EIS intensity calibration was measured before launch (Lang *et al.* 2006), but it has been subsequently revised to account for inaccuracies and sensitivity decrease with time. Unfortunately, two competing calibrations have been produced (Warren *et al.* 2014 and Del Zanna 2013 – HPW and GDZ, respectively) which provide different relative SW/LW calibration factors, which in addition depend on time in a different way. This provides a critical uncertainty to the present measurements which will also be discussed in Section 5.

3. Observations

3.1. EIS observing sequences suitable for magnetic field diagnostics

In order to test the magnetic field diagnostic technique, we produced magnetic field maps on several active regions observed during the entire EIS mission. The results we report in this paper are just a drop in the ocean, as the EIS mission has developed plenty of observing sequences which include the necessary lines to carry out magnetic field measurements. In order to help users select suitable sequences to measure the coronal magnetic field, a list of these sequences is reported in Tables 1 to 3. The vast majority of them either includes the entire Hinode/EIS spectrum, or the four Fe X and Fe XI lines we used to carry out the present diagnostics. We also report a few more where Fe XI density diagnostics is not available, but either the Fe VIII 185.2/186.6 and/or the Fe XII 186.8/195.1 ratios were available: these sequences may also be used for magnetic field diagnostics, although care must be taken in ensuring that the plasma structures observed by Fe VIII,X,XII are the same. We hope that this list will be useful to the reader to identify data sets suitable for the measurements of the magnetic field in the solar corona.

3.2. Data used in the present work

For the present work, we only selected a few observations, requiring that their fields of view include an active region, and they include all four Fe X and Fe XI lines to carry out

Acronym	FOV (arcsec ²)	Exp.time (s)	Slit (arcsec)	Full spectrum	Notes
AKATSUKI_01_SI	45×512	240	1	Y	
arm_loop_ne	82×400	25	2		
AR_velocity_map	330×304	40	1		
AR_velocity_map_v2	459×384	40	1		
AR_spectral_atlas_3	120×120	40	2	Y	
Atlas_060x512_45s	60×512	45	1	Y	
Atlas_060x512_60s	60×512	60	1	Y	
Atlas_30	120×160	30	2	Y	
Atlas_60	120×160	60	2	Y	
Atlas_120	120×160	120	2	Y	
cam_artb_cds_a_lite	200×400	10	2		
cam_artb_lite_v2	40×120	10	2		
cam_ar_limb_lite_v2	323×376	45	2		
cam_ar_temp_lite	359×400	30	2		
cam_qs_2as_velo	20×200	15	2		
cam_qs_2as_context	120×360	30	2		
cavity_dem_1	302×352	100	2		Fe VIII
CLASP-1_60x512_OBS_	60×512	60	2		
CLASP-1_60x512_CAL_	60×512	60	1		
CompS_NonMax_120	80×512	120	2		
CompS_NonMax_90	80×512	120	2		
CompS_NonMax_60	80×512	120	2		
CompS_NonMax_30	80×512	120	2		
COMSCI_QS5	10×512	5	1	Y	
Cool_loop_response	90×144	20	2		Fe VIII
Coronal_rain_1as2pos	40×256	10	1		Fe VIII
dhb_atlas_30x512	60×512	120	2	Y	
dhb_atlas_120m_30	60×160	120	2	Y	
DIAG_40x180_s0_30s	40×176	30	2		
dob_bp_slit_raster	120×160	30	2		Fe XII
DRW001_HLBRT_SCAN	5×240	60	1		
DRW001_HLBRT_V2	5×240	30	1		
DRW001_HLBRT_V3	10×240	30	1		
Eclipse_raster_2	180×176	30	2		

Table 1: Hinode/EIS observing sequences suitable for coronal magnetic field diagnostics. Sequences where density diagnostics from Fe XI is unavailable but is provided by Fe VIII and/or Fe XII ratios are indicated in the far-right column.

Acronym	FOV (arcsec ²)	Exp.time (s)	Slit (arcsec)	Full spectrum	Notes
EL_FULL_CCD_RASTER	14×512	300	2	Y	
EL_FULL_CCD_SINGLE	4×512	300	2	Y	
EL_abund_plume_SUMER	46×512	100	2		Fe VIII
EL_loop_plume_SUMER	61×512	100	2		
el_loop_diagn_sumer	61×280	50	1		
EL_WHL_CH_small	62×120	100	2		
EL_WHL_CH_LIMB	2×512		2	Y	
EL_SUMER_UVCS	2×400	150	2	Y	
EUNIS_EIS_CrossCal18	122×512	50	2		
FILL001	1×256	30	2	Y	
FELDMAN_QSCH_ATLASv1	60×304	120	2	Y	
FOCUS_STUDY	60×512	90	1		Fe XII
fullccd_sns30	2×160	30	2		
fullccd_scan_m30	120×160	30	2	Y	
fullccd_scan_l30	120×160	30	2	Y	
GDZ_300x384_S2S3_40	300×384	40	2		
GDZ_DENS_20x240_ARL1	20×240	10	2		
GDZ_DENS_20x240_ARL2	20×280	15	2		
GDZ_360x288_AR_CONT2	360×288	6	2		Fe XII
16m54s *** GDZ_PLUME1_2_300_150	300×512	150	2		
GDZ_PLUME1_2_300_50s	300×512	50	2		
gdz_off_limb1_60	487×512	60	2		
GDZ_QS1_60x512_60s	60×512	60	2		Fe XII
HH_QS_RAS_N01	60×120	60	1	Y	
HH_QS_RAS_H01	41×120	60	1	Y	
HPW001_FULLCCD_RAST	128×128	90	1	Y	
HPW001_FULLCCD_V2	26×456	90	1	Y	
HPW008_FULLCCD_RAST	128×128	25	1	Y	
HPW008_FULLCCD_V2	128×256	25	1	Y	
HPW009_FULLCCD_SAS	1×128	25	1	Y	
HPW020_VEL_FULLs1	1×512	120	1	Y	
HPW023_FULLCCD_V2	1×512	300	1	Y	
HPW023_FULLCCD_V2s2	2×512	300	2	Y	
HPW023_FULLCCD_V3s2	2×512	100	2	Y	

Table 2: Hinode/EIS observing sequences suitable for coronal magnetic field diagnostics. Sequences where density diagnostics from Fe XI is unavailable but is provided by Fe VIII and/or Fe XII ratios are indicated in the far-right column.

Acronym	FOV (arcsec ²)	Exp.time (s)	Slit (arcsec)	Full spectrum	Notes
iiap_ch_sns_v2	2×512	60	2		Fe VIII,XII
iiap_ch_ctxt_v2	120×512	60	2		
KM_FULLCCD_128x256_1slit_80sec	128×256	80	1	Y	
KM_FULLCCD_128x512_1slit_80sec	128×512	80	1	Y	
kpd_01_qs_60s	56×512	60	1		Fe VIII,XII
LANDI_SCAN_CH	60×512	240	2		
Large_CH_Map	180×512	60	2		Fe VIII,XII
madj_ech	120×512	60	2		Fe VIII,XII
madj_ech_small	24×512	60	2		Fe VIII,XII
prom_rast_v1	81×128	50	1		Fe VIII,XII
prom_rast_small_v2	4×128	25	1		Fe VIII,XII
PRY_CH_density	70×200	100	2		Fe VIII,XII
PRY_footpoints_v2	100×140	25	2		
PRY_footpoints_HI	180×512	25	2		
PRY_footpoints_HI2	180×512	25	2		
PRY_loop_footpoints	100×216	30	2		
QS_atlas_offlimb	220×512	60	1		
RED_SUM_EIS_RAST	70×200	90	1		
RED_SUM_EIS_SNS_OL	70×200	90	1		
SI001FullRast	256×256	50	1	Y	
SI002.HiCadence_AR	280×512	50	1	Y	
SI_Mercury_slit	2×256	60	2	Y	
SI_Mercury_slit_v2	2×256	20	2	Y	
SI_Venus_slit	2×256	300	2	Y	
SI_Venus_slit_v2	2×256	100	2	Y	
SYNOP001	1×256	30	1	Y	
SYNOP002	128×184	90	1	Y	
SYNOP003	300×96	45	2	Y	
SYNOP004_400x400_30	400×400	30	2		
Utz_quiet	22×160	60	1		Fe XII

Table 3: Hinode/EIS observing sequences suitable for coronal magnetic field diagnostics. Sequences where density diagnostics from Fe XI is unavailable but is provided by Fe VIII and/or Fe XII ratios are indicated in the far-right column.

the present diagnostics. We also selected a few more to check the effects of using Fe XI density and detector degradation effects later in the mission. These observations are listed in Table 4. These images were cleaned and calibrated using the standard EIS software. In addition, the detector slant was corrected so that the images obtained in the LW and SW were coaligned.

Very careful considerations were made in the choice of the intensity calibration. The GDZ calibration was determined monitoring a large number of line intensity ratios from the beginning of the EIS mission, and made extensive comparison with high accuracy line intensity measurements available in the literature. The HPW calibration attempted to improve on the GDZ calibration by relying on extensive plasma diagnostic measurements in near-isothermal quiet regions rather than on individual line intensity ratios, by tying the EIS calibration to independent measurements from the EUV Variability Experiment (EVE – Woods *et al.* 2012) and Atmospheric Imaging Assembly (AIA – Lemen *et al.* 2012) on board the Solar Dynamic Observatory (SDO – Pesnell *et al.* 2012), and also trying to calibrate the SW and LW detectors by making measurements of the Fe XXIV 192/255 line intensity ratio during flares agree with their predicted values.

No definitive conclusion can be reached regarding which of the two calibrations is most accurate. However, the GDZ calibration assumes that the LW channel did not decrease its sensitivity with time after 2012, while the HPW calibration assumes a continuous decrease. A monitoring of the Fe XIV 211.32/274.20 line intensity ratio from 2007 to 2020 indeed shows an initial decrease in relative sensitivity of the LW channel until 2012, and a subsequent flattening of the ratio (H.P. Warren, private communications), indicating that the GDZ calibration is more accurate after 2012. In this work, we preferred the GDZ calibration over the HPW one for three reasons: 1) no other systematic calibration study has been published after 2014 that provides a definitive answer on the EIS calibration; 2) the GDZ calibration is likely more accurate after 2012, and 3) for the sake of consistency. We will discuss the effects of the calibration choice in Section 5.

Line intensities were determined by summing the number of counts under the line profile and subtracting the background, determining the latter from regions of the spectrum very close to each line devoid of any other line. While such a method provides reasonably good estimates of line intensities for isolated lines (and for the 188 doublet), it needs to be tested for the 257.26 Å line. In fact, this line is surrounded by several other spectral lines which, though resolved, partially mask the wings of the Fe X transition. While the 257.26 Å line is stronger than all of them, extensive tests were run to ensure that the intensities measured in this way are within a few percent of intensities calculated by fitting Gaussian profiles to both the Fe X and the other close-by lines.

Date	Time	FOV (arcsec ²)	Exp.time (s)	Slit (arcsec)	Sequence	Full spectrum
Density comparison						
2007-Jun-02	19:56:12	128×128	25	1"	HPW008_FULLCCD_RAST	Y
2010-Jun-21	14:24:01	120×160	60	2"	ATLAS_60	Y
Magnetic field imaging						
2007-Dec-10	00:19:27	459×384	40	1"	AR_velocity_map_v2	N
2007-Dec-11	10:25:42	459×384	40	1"	AR_velocity_map_v2	N
2007-Dec-12	03:26:43	459×384	40	1"	AR_velocity_map_v2	N
2007-Dec-12	11:43:36	459×384	40	1"	AR_velocity_map_v2	N
2007-Dec-13	12:18:42	459×384	40	1"	AR_velocity_map_v2	N
2007-Dec-15	00:13:49	459×384	40	1"	AR_velocity_map_v2	N
2007-Dec-15	18:15:49	459×384	40	1"	AR_velocity_map_v2	N
2007-Dec-18	00:10:49	459×384	40	1"	AR_velocity_map_v2	N
2007-Dec-18	18:13:41	459×384	40	1"	AR_velocity_map_v2	N
Time variation magnetic field						
2008-Jan-10	18:07:32	180×512	25	2"	PRY_footpoints_HI	N
2008-Jan-10	22:51:03	180×512	25	2"	PRY_footpoints_HI	N
2008-Jan-11	00:16:33	180×512	25	2"	PRY_footpoints_HI	N
2008-Jan-11	00:57:03	180×512	25	2"	PRY_footpoints_HI	N
2008-Jan-11	01:37:32	180×512	25	2"	PRY_footpoints_HI	N
2008-Jan-11	02:18:02	180×512	25	2"	PRY_footpoints_HI	N
2008-Jan-11	03:39:02	180×512	25	2"	PRY_footpoints_HI	N
2008-Jan-11	04:31:24	180×512	25	2"	PRY_footpoints_HI	N
2008-Jan-11	05:30:47	180×512	25	2"	PRY_footpoints_HI	N
2008-Jan-11	06:11:17	180×512	25	2"	PRY_footpoints_HI	N
2008-Jan-11	07:11:06	180×512	25	2"	PRY_footpoints_HI	N
2008-Jan-12	13:20:33	180×512	25	2"	PRY_footpoints_HI	N
2008-Jan-12	14:01:04	180×512	25	2"	PRY_footpoints_HI	N
2008-Jan-12	14:41:34	180×512	25	2"	PRY_footpoints_HI	N
2008-Jan-12	15:22:04	180×512	25	2"	PRY_footpoints_HI	N
2008-Jan-14	12:00:33	180×512	25	2"	PRY_footpoints_HI	N
2008-Jan-14	13:21:30	180×512	25	2"	PRY_footpoints_HI	N
2008-Jan-14	14:02:00	180×512	25	2"	PRY_footpoints_HI	N
2008-Jan-14	14:42:30	180×512	25	2"	PRY_footpoints_HI	N
2008-Jan-14	21:30:02	180×512	25	2"	PRY_footpoints_HI	N
2008-Jan-14	22:10:31	180×512	25	2"	PRY_footpoints_HI	N
2008-Jan-15	00:18:32	180×512	25	2"	PRY_footpoints_HI	N
2008-Jan-15	11:24:25	180×512	25	2"	PRY_footpoints_HI	N
2008-Jan-15	12:04:54	180×512	25	2"	PRY_footpoints_HI	N
2008-Jan-15	12:45:24	180×512	25	2"	PRY_footpoints_HI	N
LW detector degradation effects						
2014-Mar-16	12:15:26	120×160	60	2"	ATLAS_60	Y
2016-Oct-25	11:33:15	120×160	30	2"	ATLAS_30	Y
2018-Dec-28	19:10:40	120×160	60	2"	ATLAS_60	Y

Table 4: Hinode/EIS observations used in the present work.

4. Results

Since this technique simply consists in determining the excess emission in the 257.26 Å, in principle it can be applied to all the EIS observing sequences that include this line, a reference Fe X line, and a suitable density diagnostic line pair to measure the electron density with. While not all EIS observing sequences have all these required lines, observations that include them span the entire EIS mission. As such, applying this technique to this wealth of data is beyond the scope of this work; here we focus on presenting a few examples of this application, and discuss their uncertainties.

4.1. Magnetic field morphology

An example of the application of the Fe X magnetic field diagnostic technique is shown in Figures 2 to 4. This set of observations, carried out between 2007 December 10 and 18, follows AR10978 as it rotated on the solar disk until reaching the west limb. Despite the size and complexity, this active region was relatively quiet and hosted only a few C-class flares, although none of them took place while the observations were taken. Figures 2 to 4 show a snapshot of the Fe X 184.54 Å intensity map on the left column and the magnetic field map obtained with the present MIT diagnostic technique on the right column for each of the nine observation times. There are a few things to notice.

First, the magnetic field structures shown in the figures closely follow the intensity maps of the Fe X line, as expected both on the grounds of better SNR, and because the magnetic field confines the active region plasma maintaining it at higher density and temperature than the surrounding ambient plasma. Observations closer to disk center allow the reconstruction of several different loop structures connecting magnetic field of opposite polarities, although the tallest loops become too faint as they rise to large altitude, such as those in the SW portion of AR10978 in Figure 2, so that they can not be observed for the entirety of their length.

Second, even if the observations were taken only a few hours apart from each other, the magnetic field shows significant evolution, both in morphology and in strength, with magnetic loops changing position, appearing or disappearing from one observation to the next. This is consistent with the variability of line intensities, and directly links the evolution of the field strengths with the plasma properties inside magnetic structures.

Third, the strength of the magnetic field ranges from ≈ 100 G to more than 300 G, being stronger in low-lying loops and weaker in larger loops. However, it is unclear whether the lower strength in large loops (leading to disappearance of the loop themselves at large

heights) is due to a real weakening of the field with height, or to a lower SNR. During the transit of AR10978 from disk center to the limb, the magnetic field strength steadily increases, consistently with the active region beginning to be more active and starting to host small C-class flares from December 13 (three C-class flares, the strongest of which a C4.5 flare) until it turned behind the limb on December 19.

The variability of the magnetic field strength with height can be best monitored in Figure 4, where AR10978 is observed close to, or at the limb. In these images, the strongest magnetic field (reaching and exceeding 300 G) is concentrated in the lowest-lying structures, closest to the surface, while taller loops have weaker fields, in the 100-250 G range. The tallest loops visible in the Fe x 184.54 Å image are barely visible in the magnetic field strength image, indicating that their magnetic field is either too weak to be detected, or the SNR is too low to allow this diagnostic technique to be effective. However, the very few closed loop structures whose magnetic field strength is measurable at the limb for seemingly the whole loop length show a slow varying magnetic field, which becomes weaker with height.

4.2. Magnetic field evolution

Magnetic field strength maps also allow us to monitor the short term evolution of individual structures in an active region. An example of this is reported in Figure 5, where a weak active region with no number, which was trailing AR10980 at the solar equator, was repeatedly observed from January 10 to 15, 2008. During this time, the active region was observed for a total of 25 times, and showed a marked evolution which led to no flares.

The high resolution of the EIS spectrometer allows us to identify individual plasma structures and monitor their evolution with time: we have identified the footpoint of a system of active region fanning loops, which is highlighted in Figure 5 (top) by the black rectangle, and measured the magnetic field of the selected box as a function of time. The magnetic field of this region looked very weak, as a pixel-by-pixel map of the coronal magnetic field of this region indicated the presence of a measurable field, with a very poor SNR. In order to increase the SNR and attempt to measure the magnetic field strength in such a weak region, we have summed all the counts for each spectral line within the box and applied the magnetic field diagnostic technique to the total line intensities.

Results are shown in Figure 5 (bottom). The uncertainties of each measurement are given by the uncertainty in the relative calibration between the EIS LW and SW channel, estimated to be 50%. The magnetic field is very weak, on the order of 30-150 G, and shows a vague tendency to decrease with time. Results tend to show some variability within the same

cluster of observations (a couple of observations gave zero magnetic field strength), indicating that we are sampling the sensitivity limits of the present magnetic field diagnostic technique. This means that it will be very difficult to measure magnetic fields in the quiet Sun and even less in coronal holes, where magnetic field strengths are smaller; the only places where such a measurement may be attempted with some hope of success are low-latitude locations at the solar limb, where the very long line of sight intercepts more plasma, increasing the SNR.

Another difficulty at carrying out such measurements is the evolution of the plasma structures themselves, and the different viewing angle as they rotate on the solar disk. Both properties makes the identification of an individual structure and its monitoring over long periods of time difficult and adds to the uncertainty of the measurement.

5. Uncertainties

5.1. Energy level separation

Despite the great potential for magnetic field diagnostics, the present technique has several uncertainties of different nature. The first and most important is the intrinsic uncertainty in the calculation of the Einstein coefficient A_{MIT} for the magnetically-induced transition. As discussed by Si *et al.* (2020a), to first order we can assume

$$A_{MIT} \propto \frac{B^2}{(\Delta E)^2} \quad (3)$$

where ΔE is the energy separation between the two ${}^4D_{5/2,7/2}$ levels generating the 257.26 Å doublet. Measuring this energy separation is difficult because it is very small, and there are only a few spectral lines available that can be utilized, all very close in wavelength. Separating the two lines at 257.26 Å is essentially impossible as their separation is just a few mÅ, way below the resolution of the EIS instrument; also the line width in the corona is way larger than this separation.

ΔE can be measured using transitions where the ${}^4D_{5/2,7/2}$ levels are the lower levels of transitions coming from the same upper level forming a doublet, as used by Judge *et al.* (2016). A few lines are available for this purpose. No laboratory or solar observations are available for a doublet at around 3500 Å, which would provide a separation of 0.65 Å, the 2935 Å doublet, and another doublet at 1611 Å. Only a few observations in the UV are available for the only other three transitions remaining: at around 1918 Å, 1603 Å, and 1028 Å; the separation of the two lines being larger at longer wavelengths. Judge *et al.*

(2016) utilized S082 spectra taken at the solar limb to measure the 1603 Å doublet separation through double Gaussian fitting, finding $\Delta E = 3.7 \pm 2.9 \text{ cm}^{-1}$, so that the uncertainty is around 80%. This uncertainty makes the technique capable of giving only the order of magnitude of the magnetic field strength.

More recently, Landi *et al.* (2020) have utilized the deep exposure of the quiet solar limb made with the high-resolution SoHO/SUMER spectrometer (Wilhelm *et al.* 1995) that provided the SUMER off-disk spectral atlas (Curdt *et al.* 2004); in this observation, the Fe X 1463.49 Å was used to constrain the line width for all Fe X lines, helping reduce the ΔE uncertainty. Landi *et al.* (2020) determined a value of $2.29 \pm 0.50 \text{ cm}^{-1}$. This uncertainty, at 20% level, greatly reduces the intrinsic uncertainty of any measurement of the magnetic field (see Equation 3).

5.2. Electron density

In order to determine the *MIT/M2* branching ratio from the observations, it is necessary to determine the plasma electron density independently. This can in principle be done using Fe X transitions, whose emission is generated by the same plasma emitting the 257.26 Å line. Si *et al.* (2020b) suggest the use of the two strong Fe X transitions at 175.26 Å and 174.53 Å: this choice is the most sensible, but these two lines are observed at the edge of the EIS SW detector where the sensitivity is very low, and their intensities are highly uncertain. No other Fe X line ratios with bright lines with high SRN is available in the EIS wavelength range. The next best solution is to utilize lines from ions formed at similar temperatures, and the best choice is Fe XI, as both Fe X, XI are ions formed in the corona only, while Fe IX has a strong contribution from colder, upper transition region plasmas which makes its emission contaminated by plasmas likely not contributing to Fe X. Besides, Fe IX density sensitive lines in the EIS spectrum are weaker and more difficult to observe and disentangle from nearby transitions. On the contrary, Fe XI provides strong, isolated lines that are routinely observed by the EIS spectrometer: the 182.17 Å and the 188.22+188.30 Å doublet. The latter is actually a partially resolved doublet, but it is very strong and sufficiently isolated to make it very easy to measure.

However, using density measurements from another ion raises additional uncertainties: the emitting plasmas might not be the same, and thus the density measured by the two ions can be different. Figures 6 and 7 show intensity maps of two active regions in the Fe X 184.54 Å line and Fe XI 188.2 Å doublet, showing that indeed the two ions sample the same plasmas. These observations were taken as examples because they also included the 174.54 Å and 175.26 Å lines, so that differences in the density values and their spatial

distribution could be checked. Both active regions clearly show the difficulty in observing the two Fe X 174.54 Å and 175.26 Å lines, due to the poor SNR, which is amplified in their ratio; still, the spatial distribution of the densest areas is the same as with the Fe XI density ratio. A detailed comparison of density measurements over restricted areas show that these two ratios are within $\Delta \log N_e \approx 0.1$ in the brightest areas where the magnetic field measurements will be most accurate. Density values are in the $\log N_e = 9.0 - 9.6$ range, where also the intensity ratios in Equations 1 and 2 are density sensitive, so that electron density may indeed contribute to the overall uncertainty in the measurement of the magnetic field strength.

5.3. Intensity calibration

Calibration is another source of uncertainty of critical importance. The reason is that all the strongest Fe X lines are located in the SW channel, while the magnetically sensitive 257.26 Å is located in the LW channel, so that the relative calibration of the two is uncertain. This uncertainty will directly propagate into the determination of both I_{MIT} and I_{M2} in Equations 1 and 2. Two independent studies (HPW and GDZ) have been carried out to determine the in-flight EIS intensity calibration and compared it with the pre-launch one, from Lang *et al.* (2006).

Results showed that the pre-flight sensitivity of the LW channel was overestimated, but GDZ and HPW disagreed on the amount. Even more importantly, the LW channel showed a degradation with time relative to the SW channel, which directly impacts the present diagnostic technique. The wavelength dependence of the effective areas within each channel was largely the same as the pre-flight calibration, with the exception of the shortest wavelength of the SW channel (GDZ) or both ends of the SW channel (HPW): in both cases, the use of the 174.53 Å line for the measurement of the magnetic field proposed by Si *et al.* (2020b) is significantly affected. Also, contradictory results were obtained when comparing the EIS absolute calibration with both the EVE instrument on board SDO, and the rocket EUNIS flight (Wang *et al.* 2011).

These uncertainties and discrepancies directly affect the present diagnostic technique. An example of calibration-related uncertainties is shown in Figures 8 and 9, which display some of the data shown in Figures 2 to 4. The left panels show Fe X 184.54 Å intensity maps, and the middle and right panels show magnetic field strength measurements obtained with HPW calibration (middle panels) and GDZ calibration (right panels). As the scale of the magnetic field in both panels is the same, differences are apparent, with the HPW calibration leading to higher values for the stronger magnetic field, and giving zero magnetic

field strength for regions where the GDZ calibration provides small, but measurable values of the magnetic field.

It is important to note that the uncertainties in the intensity calibration have a much more limited impact on the determination of the plasma electron density, because this parameter is measured using intensity ratios from lines close in wavelength, so that any uncertainty is minimized. Nonetheless, we strongly urge the EIS instrument team to resume efforts to determine the EIS sensitivity for the entire duration of the mission.

5.4. EIS detector sensitivity degradation

Figure 10 shows the results of applying the magnetic field diagnostic technique to data sets taken in later stages of the EIS mission, where the instrument sensitivity has already significantly decreased, especially for the LW channel where the magnetically sensitive 257.26 Å line resides. Those results were obtained on full EIS spectra obtained with 60s exposure time and the 2" slit, a combination that at the beginning of the EIS mission ensured a very high SNR ratio. While the intensity image has still high quality, the SNR ratio has degraded significantly, and the application of the diagnostic techniques, that needs a high SNR, gives results plagued by both instrumental effects and significantly more noise than earlier in the mission. Results can still be reliably obtained (especially considering that no rebinning or other correction was applied to these data sets shown in Figure 10) but the degradation of the instrument is apparent.

5.5. Atomic data

The accuracy of the atomic data is also of critical importance for the present study. We have used CHIANTI version 9.0 to calculate line emissivities for all the levels of Fe X as well as, when used for density diagnostics, Fe XI. The original sources for these data are Del Zanna *et al.* (2010, 2013) for Fe XI, and Del Zanna *et al.* (2012) for Fe X. In both cases large scale models for the atomic target were considered. These works provided both energy levels, Einstein coefficients for spontaneous decay (A-values) and Maxwellian-averaged collision strengths.

The accuracy was benchmarked with observations from a number of laboratory, rocket, and space instrument measurements (Del Zanna 2011), as well as by Del Zanna *et al.* (2010, 2013) for Fe XI, Del Zanna *et al.* (2012) for Fe X, and more recently by Landi (2020, in preparation, both ions). These studies, using many observations from a number of different

instruments, found that the intensities of the spectral lines used in this work for magnetic field diagnostics were in excellent agreement with observations. Most importantly, most of the observations used to test Fe X were taken from quiescent spectra where the MIT transition is expected to be negligible, so that the ambient magnetic field did not affect the results.

Still, any uncertainty in the atomic data will directly affect magnetic field measurements. In particular, at typical electron densities of active regions both the ${}^4D_{5/2,7/2}$ levels are populated mostly by radiative cascades from higher levels, so that the accuracy of both collision excitation rates and Einstein coefficients involving levels different than the ${}^4D_{5/2,7/2}$ is of great importance.

As an example, recently Wang *et al.* (2020) published a new, large scale calculation for energy levels and A-values of Cl-like ions which also included data for Fe X. The much more extended model adopted in this calculation resulted in significant differences in the lifetimes and A values of many of the levels in the $3s^23p^43d$ configuration; as the ${}^4D_{5/2,7/2}$ levels are mostly populated by cascades from $3s^23p^43d$ levels with higher energy, these differences can have significant effects on their level population and therefore their line intensities. In order to assess the relevance of this effect, we have repeated all the measurements using an Fe X model that combined the Wang *et al.* (2020) Einstein coefficients with the CHIANTI 9 collisional data, finding that the measured magnetic field strengths increased by 20-30% with this hybrid model over the values obtained utilizing the CHIANTI 9 data for both collisional and radiative data.

Unfortunately, Wang *et al.* (2020) only provided radiative data, lifetimes and energy levels, but no collisional data, so that a self-consistent calculation of line intensities could not be done. This comparison only underscore the need of new, large-scale calculations of Fe X collisional data using atomic models of the same accuracy as Wang *et al.* (2020). This is of course a formidable task, due to the added complexity in computing collision strengths, as well as other atomic properties involving continuum states, compared to rates in bound-bound transitions.

6. Discussion and future work

The present work illustrates the potential of a new diagnostic technique that allows the measurement of the magnetic field strength in active regions utilizing bright Fe X and Fe XI lines commonly observed by the Hinode/EIS satellite. This technique, which is based on a peculiar property found uniquely in two, near-degenerate Fe X atomic levels, opens a new window on one of the most important, and less measured quantities in solar physics: the

coronal magnetic field.

The potential of this new diagnostic technique lies in two basic facts: 1) that the coronal magnetic field determines all the critical processes at the heart of coronal heating, plasma confinement, and of the solar activity events (flares and CMEs) that give rise to Space Weather and to all the adverse effects it has on human assets on the ground and in space; 2) it can be applied to an existing data set spanning from 2007 to 2020 (as of this writing), extending for more than one full solar cycle (including the anomalously weak minimum of solar cycle 24 in 2007-2009), and covering a large number of active regions, flares, and even coronal mass ejections. Thus, this new diagnostic technique opens the door for a whole new field of studies.

The importance of this technique is all the more enhanced by the development and deployment of the next generation ground based observatories which will be able to measure the coronal magnetic field orientation and line-of-sight component at the solar limb: DKIST and UCoMP. When combined together at the limb, EIS, DKIST and UCoMP observations will enable us to reconstruct the full magnetic field in coronal active regions, providing for the first time an observable of incalculable value for local and global models of active regions and of the solar corona. Furthermore, unlike UCoMP and DKIST, EIS can measure the coronal magnetic field on the disk, thus allowing the monitoring of active region fields as they transit across the disk: this capability enables the search of magnetic precursors to flares and CMEs, hopefully paving the way towards reliable Space Weather forecasting systems. Furthermore, this technique allows to match magnetic field measurements to the determination of other properties that can be obtained with spectral lines from Fe X and other elements with the same instrument, providing a very complete characterization of active region plasmas.

In this work we present a few examples of the application of this technique to EIS observations taken at different times, monitoring the morphology, strength and evolution of active region magnetic fields. We find that the magnetic field strength in non-flaring active regions evolves both in morphology and strength over time, and its value ranges from a few tens to a few hundred Gauss. The present technique is also able to provide 2D maps of the magnetic field in the plasma that emit Fe X line intensities.

Even more importantly, we present a list of EIS observing sequences whose data include all the lines necessary for the application of this diagnostic technique, and a few more that include density diagnostic line pairs from other ions that could also be used in some situations. We hope that this list will help the solar community navigate the immense set of EIS data and more easily find data to measure the coronal magnetic field.

However, this technique comes with limitations, that need to be overcome. The energy

separation between the Fe X $4D_{5/2,7/2}$ levels needs to be determined with even higher accuracy than obtained by Landi *et al.* (2020), so that the intrinsic uncertainty on the A_{MIT} value can be minimized. Also, the calibration of the EIS instrument needs to be determined both as a function of wavelength and as a function of time across the entire EIS mission, so that uncertainties related to the relative calibration within, and between, the SW and LW detectors can be minimized as well. Also, we encourage the atomic physics community to improve on the radiative and collisional data for Fe X over what is currently available, in order to minimize the effects of errors in the atomic and collision parameters on the measured magnetic field.

E. Landi was supported by NSF grants AGS 1408789, 1460170, and NASA grants NNX16AH01G, NNX17AD37G and 80NSSC18K0645. The authors would like to thank Dr. H.P. Warren for helpful discussions on the EIS intensity calibration.

REFERENCES

- Beiersdorfer, P. *et al.* 2003, Phys. Rev. Lett. 90, 235003
- Brosius, J.W., Landi, E., Cook, J.W., *et al.* 2002, ApJ, 574 453
- Brosius, J.W., & White, S.M. 2006, ApJ, 641, L69
- Cranmer, S.R. 2009, LRSP, 6, 3
- Culhane, J.L., Harra, L.K., James, A.M., *et al.* 2007, Solar Physics, 243, 19
- Curdt, W., Landi, E., & Feldman, U. 2004, A&A, 427, 1045
- De Moortel, I., Pascoe, D.J., Wright, A.N., & Hood, A.W. 2016, Plasma Physics and Controlled Fusion, 58, 014001
- Del Zanna, G., Storey, P. J., & Mason, H. E. 2010, A&A, 514, A40
- Del Zanna, G. 2011, A&A, 514, A41
- Del Zanna, G., Storey, P.J., Badnell, N.R., Mason, H. E., 2012, A&A, 541, A90
- Del Zanna, G., Storey, P.J., 2013, A&A, 549, A42
- Del Zanna, G., & Mason, H.E. 2018, LRSP, 15, 5

- Dere, K.P., Landi, E., Mason, H.E., Monsignori Fossi, B.C., & Young, P.R. 1997 *A&AS*, 125, 149
- Dere, K.P., Del Zanna, G., Young, P.R., Landi, E., & Mason, H.E. 2019, *ApJS*, 241, 22
- Feldman, P., Levitt, M., Manson, S., & Novick, R. 1967, *Physica* 33, 278
- Gombosi, T.I., van der Holst, B., Manchester, W.B. IV, & Sokolov, I.V. 2018, *LRSP*, 15, 4
- Judge, P.G., Hutton, R., Li, W. & Brage, T. 2016, *ApJ*, 833, 185
- Kosugi, T., Matsuzaki, K., Sakao, T., *et al.* 2007, *Solar Physics*, 243, 3
- Kramida, A., Ralchenko, Yu., Reader, J., and the NIST ASD Team, 2019, NIST Atomic Spectra Database (version 5.7.1), [Online]. Available: <https://physics.nist.gov/asd> [Thu Jul 02 2020]. National Institute of Standards and Technology, Gaithersburg, MD. DOI: <https://doi.org/10.18434/T4W30F>
- Landi, E., Hutton, R., Brage, T., & Li, W. 2020, *ApJ*, *submitted*
- Landi, E. 2020, *ApJ*, *submitted*
- Lang, J., Kent, B., Paustian, W., *et al.* 2006, *Applied Optics*, 45, 8689
- Lemen, J.R., Title, A.M., Akin, D.J., *et al.* 2012, *Sol. Phys.*, 275, 17
- Li, W. *et al.* 2015, *ApJ*, 807, 69
- Li, W. *et al.* 2016, *ApJ*, 826, 219
- Nindos, A., White, S.M., Kundu, M.R., & Gary, D.E. 2000, *ApJ*, 533, 1053
- Pesnell, W.D., Thompson, B.J., & Chamberlin, P.C. 2012, *Sol. Phys.*, 275, 3
- Phillips, K.J.H., Feldman, U., & Landi, E. 2008, *Ultraviolet and X-ray Spectroscopy of the Solar Atmosphere*, Cambridge Astrophysics Series 44, Cambridge University Press, Cambridge, UK
- Scherrer, P.H., Bogart, R.S., Bush, R.I., *et al.* 1995, *Solar Physics*, 162, 129
- Scherrer, P.H., Schou, J., Bush, R.I., *et al.* 2012, *Solar Physics*, 275, 207
- Si, R., Li, W., Brage, T., & Hutton, R. 2020a, *J. Phys. B*, 53, 095002
- Si, R., Brage, T., Li, W., Grumer, J., Li, M., & Hutton, R. 2020b, *ApJL*, *in press*

- Stakhiv, M., Lepri, S.T., Landi, E., *et al.* 2016, ApJ, 829, 117
- Stakhiv, M., Landi, E., Lepri, S.T., *et al.* 2015, ApJ, 801, 100
- Suematsu, Y., Tsuneta, S., Ichimoto, K., *et al.* 2008, Solar Physics, 249, 197
- Tomczyk, S., Card, G.L., Darnell, T., *et al.* 2008, Solar Physics 247, 411
- Tomczyk, S., Landi, E., *et al.* 2020, Solar Physics, *in preparation*
- Wang, T., Thomas, R.J., Brosius, J.W., *et al.* 2011, ApJS, 197, 32
- Wang, K. Jönsson, P., Del Zanna, G., Godefroid, M., Chen, Z.B., Chen, C.Y., & Yan, J.
2020, ApJSS, 246, 1
- Webb, D.F. & Howard, T.A. 2012, LRSP, 9, 3
- White, S.M., Kundu, M.R., Garaimov, V.I., *et al.* 2002, ApJ, 576, 505
- Wilhelm, K., Curdt, W., Marsch, E., *et al.* 1995, Solar Physics, 162, 189
- Woods, T.N., Eparvier, F.G., Hock, R. Hock, *et al.* 2012, Sol. Phys., 275, 115

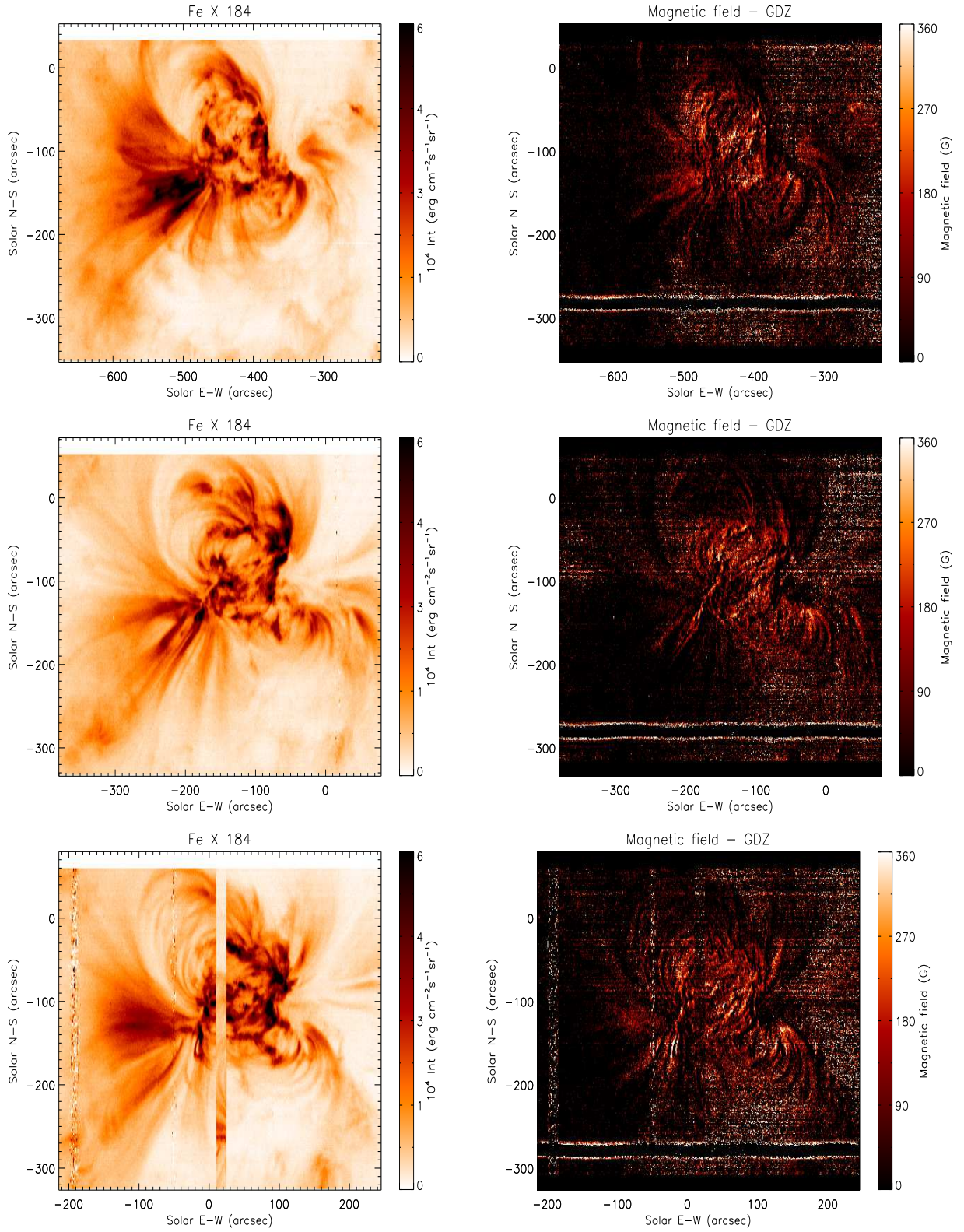


Fig. 2.— AR10978 maps on December 2007: Fe x 184.54 Å intensity (left) and magnetic field strength (right). Observation days are 10 December (00:19:27 UT, top), 11 December (10:25:42 UT, middle) and 12 December (03:26:43 UT, bottom).

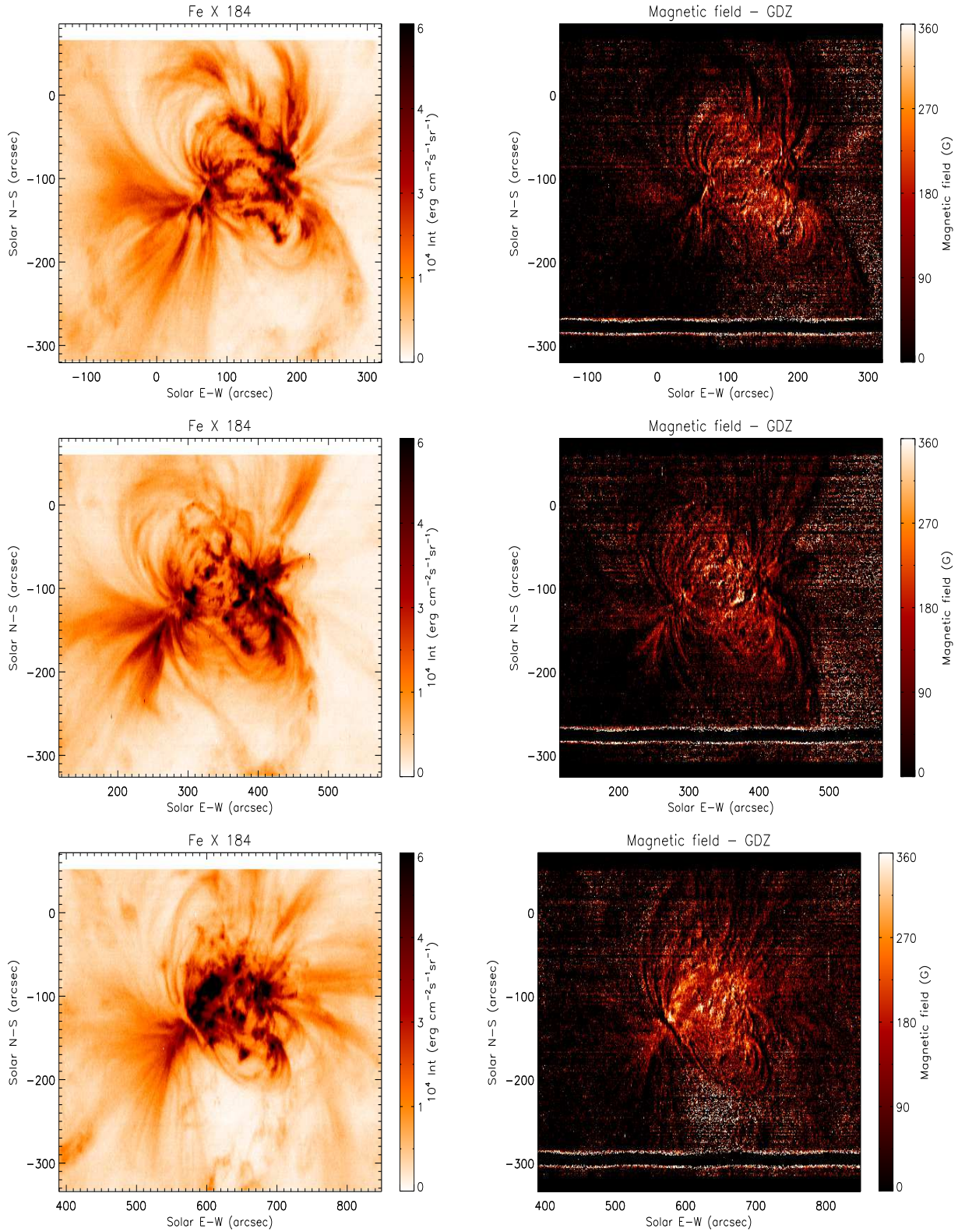


Fig. 3.— AR10978 maps on December 2007: Fe x 184.54 Å intensity (left) and magnetic field strength (right). Observation days are 12 December (11:43:36 UT, top), 13 December (12:18:42 UT, middle) and 15 December (00:13:49 UT, bottom).

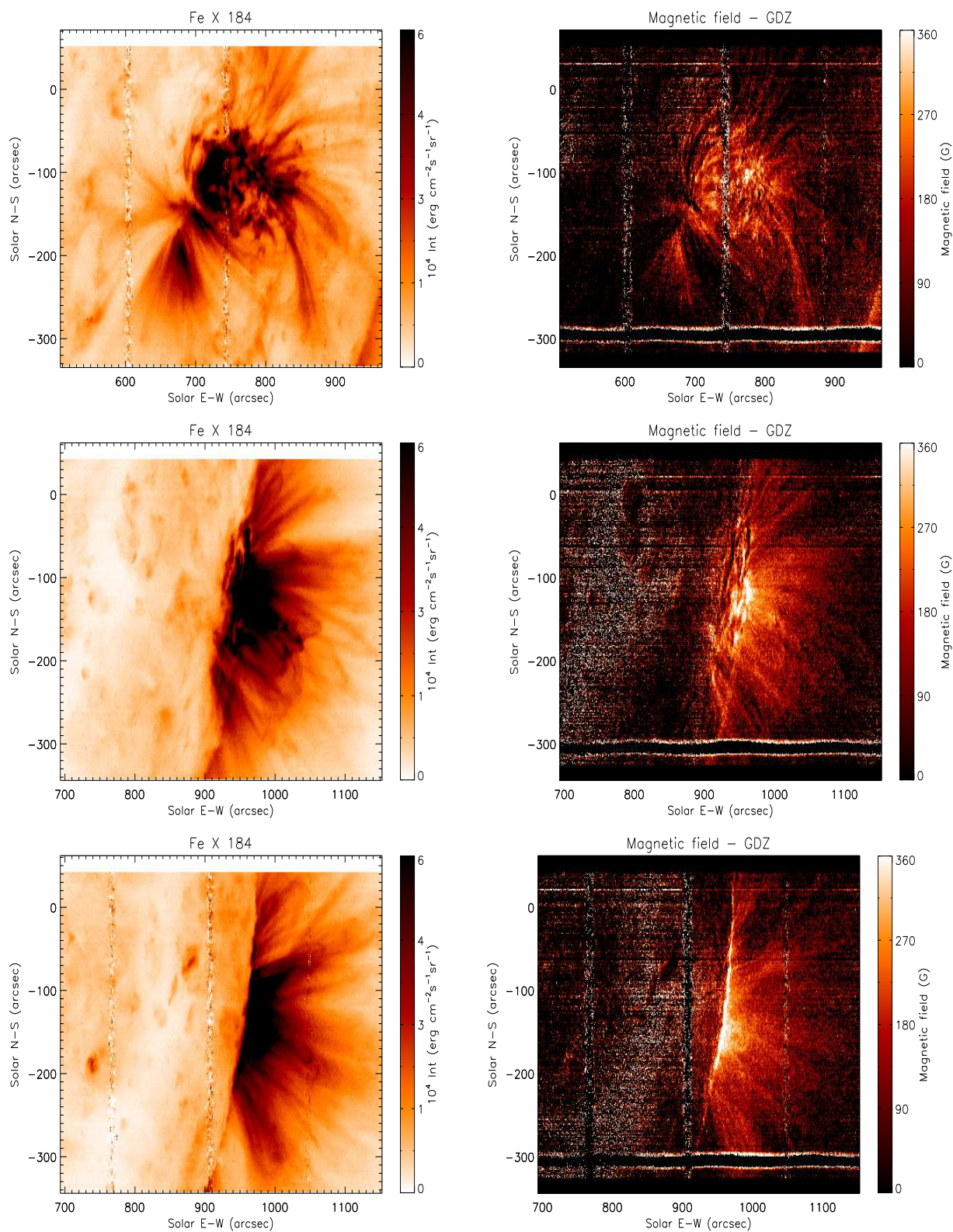


Fig. 4.— AR10978 maps on December 2007: Fe x 184.54 Å intensity (left) and magnetic field strength (right). Observation days are 15 December (18:15:49 UT, top), and 18 December (00:10:49 UT, middle and 18:13:41 UT, bottom).

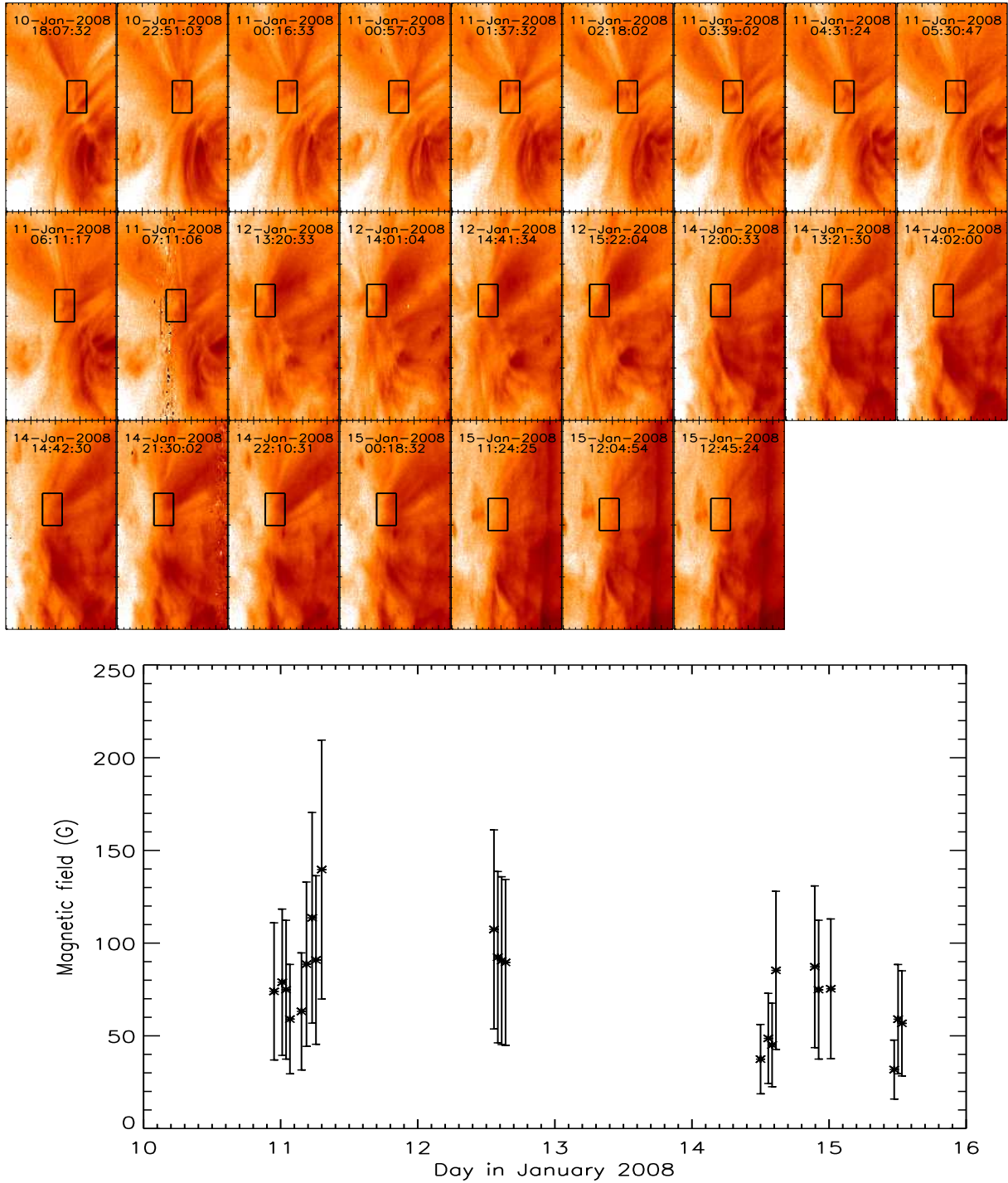


Fig. 5.— Magnetic field measurement for a weak active region observed between January 10 to 15, 2008. Intensities have been averaged over the reported boxes for each of the observations, and the magnetic field measurement has been carried out on the averaged intensities. **Top panel:** Fe X 184.54 Å intensity maps of a portion of the active region including the footpoints of fanning loops. **Bottom panel:** magnetic field strength measurements as a function of time.

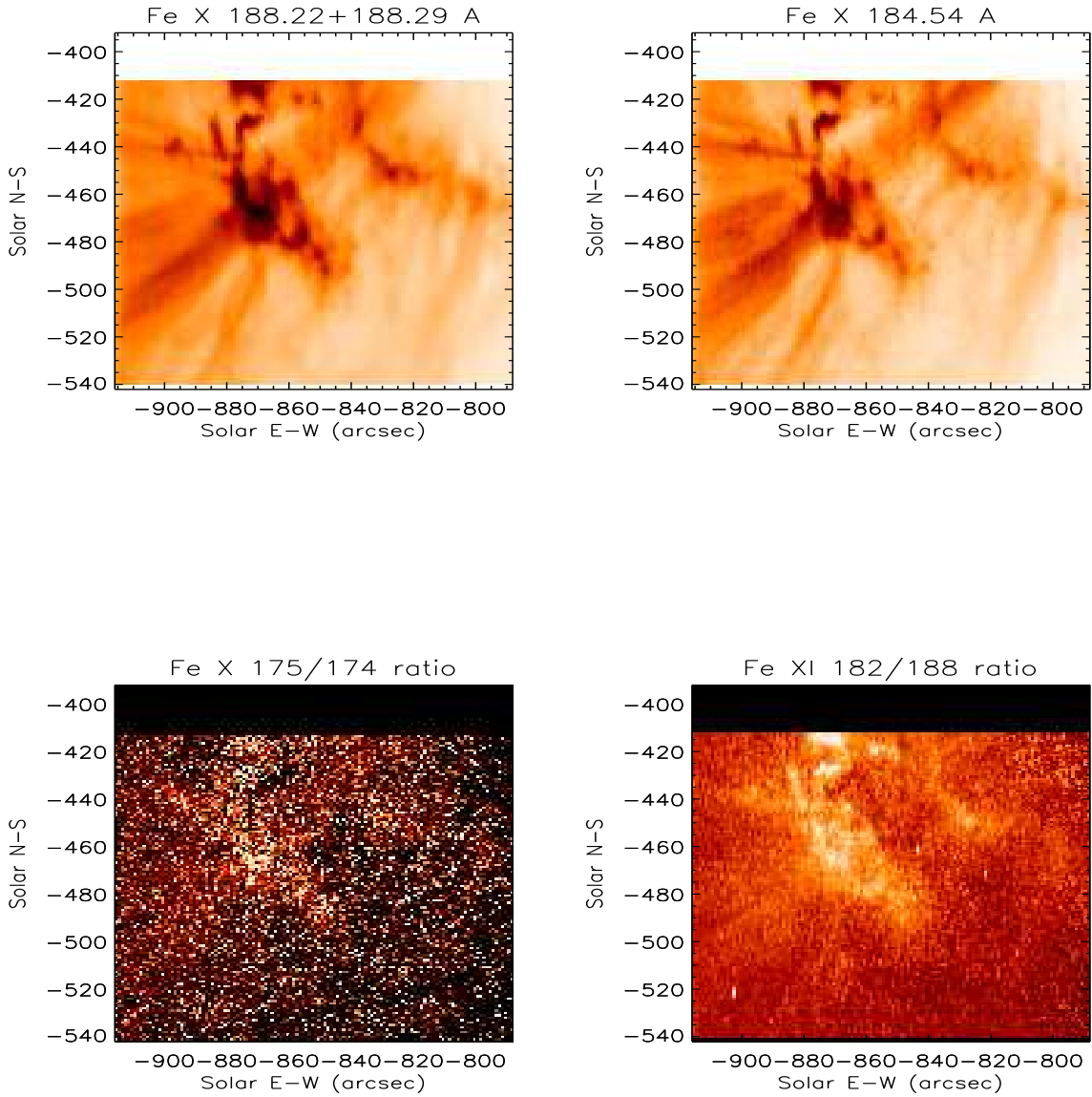


Fig. 6.— EIS observations of AR10960 observed on June 2, 2007. **Top:** intensity maps obtained with the Fe XI 188.2 Å doublet and the Fe X 184.54 Å line. **Bottom left:** Density map obtained with the Fe X 175.26/174.54 intensity ratio; **Bottom right:** Density map obtained with the Fe XI 182/188 intensity ratio.

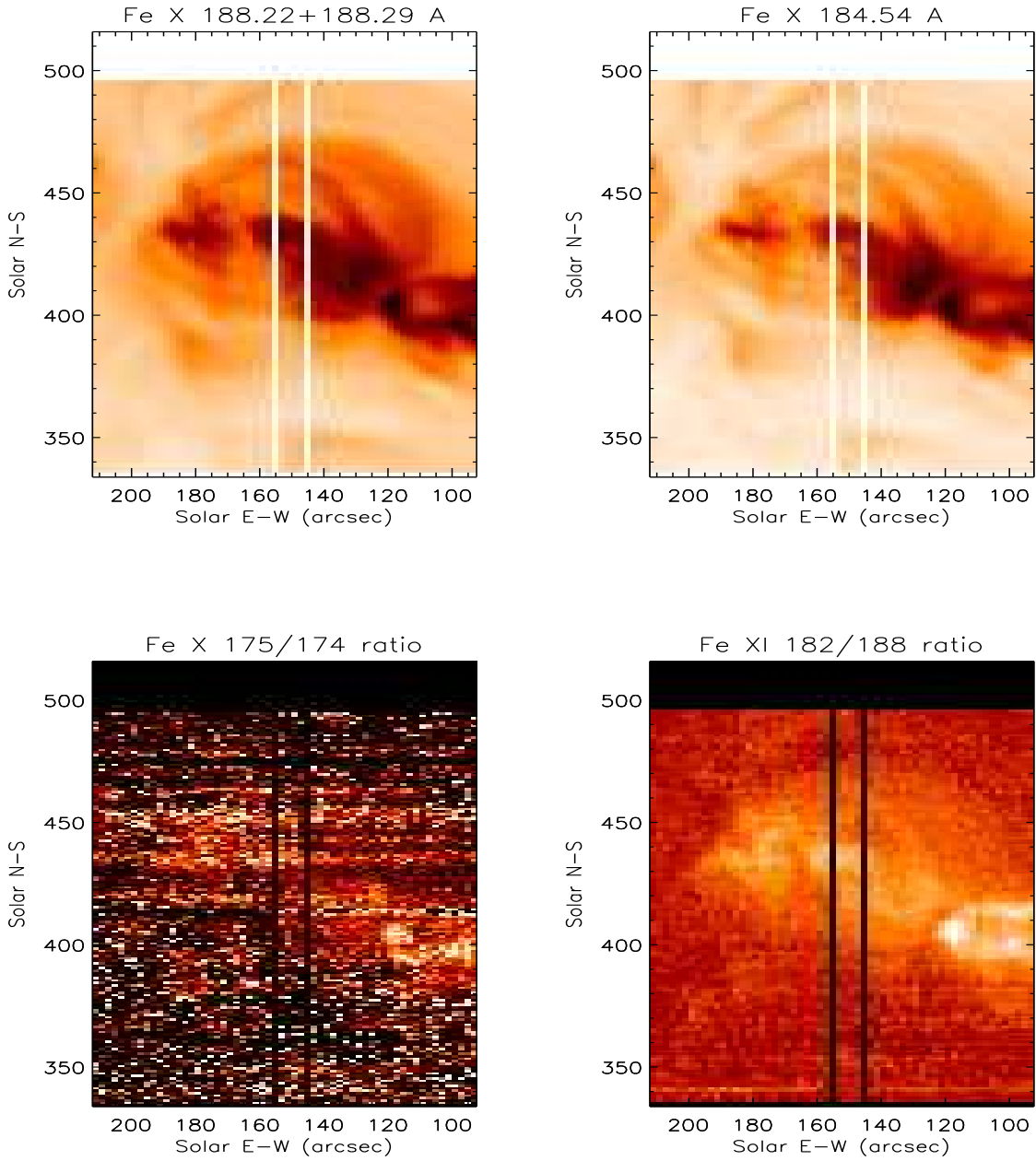


Fig. 7.— EIS observations of AR11082 on June 2, 2007. **Top:** intensity maps obtained with the Fe XI 188.2 Å doublet and the Fe X 184.54 Å line. **Bottom left:** Density map obtained with the Fe X 175.26/174.54 intensity ratio; **Bottom right:** Density map obtained with the Fe XI 182/188 intensity ratio.

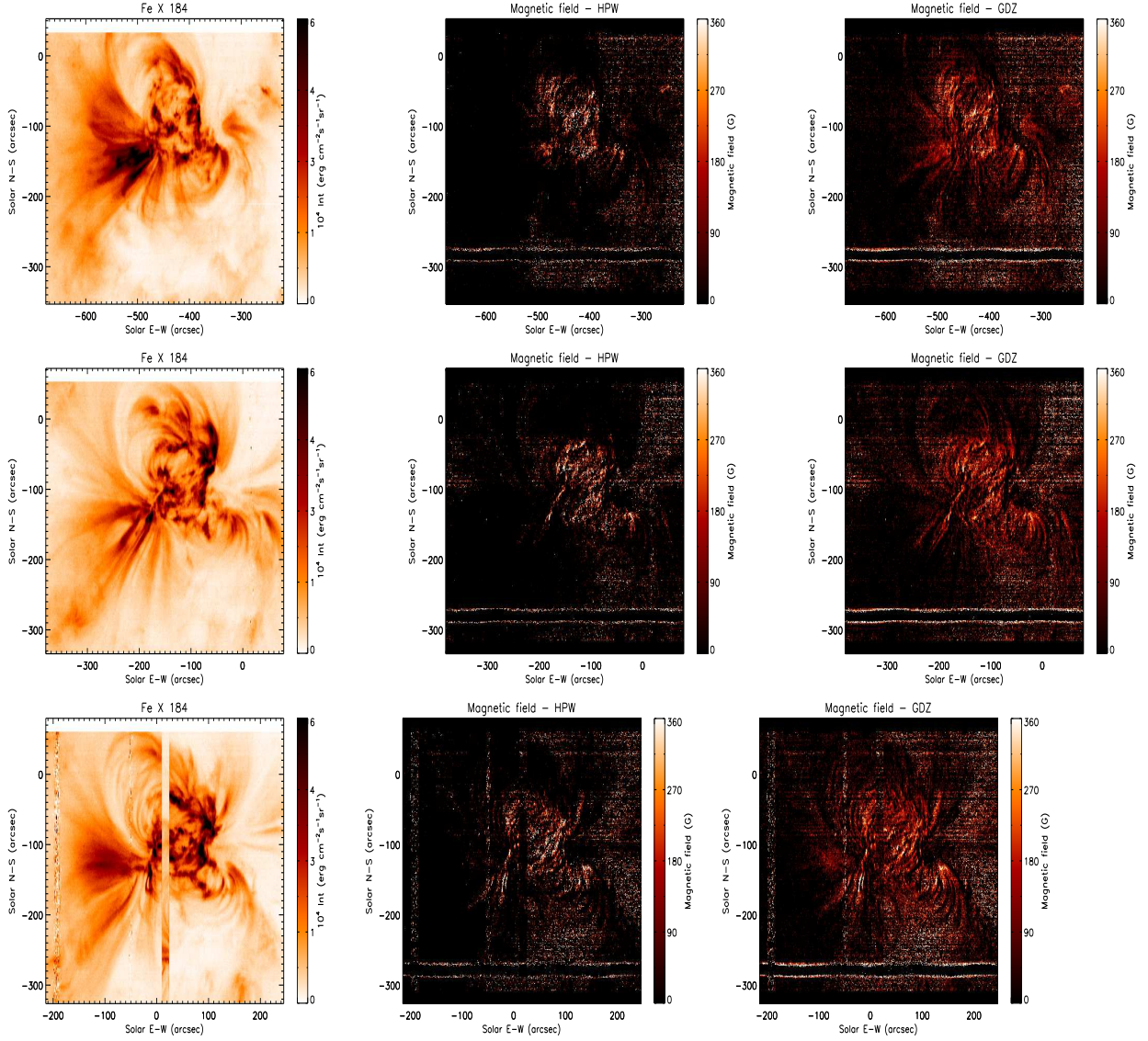


Fig. 8.— Comparison of magnetic field diagnostic results obtained with the HPW calibration (middle panels) and the GDZ calibration (right panels) from observations of AR10978.

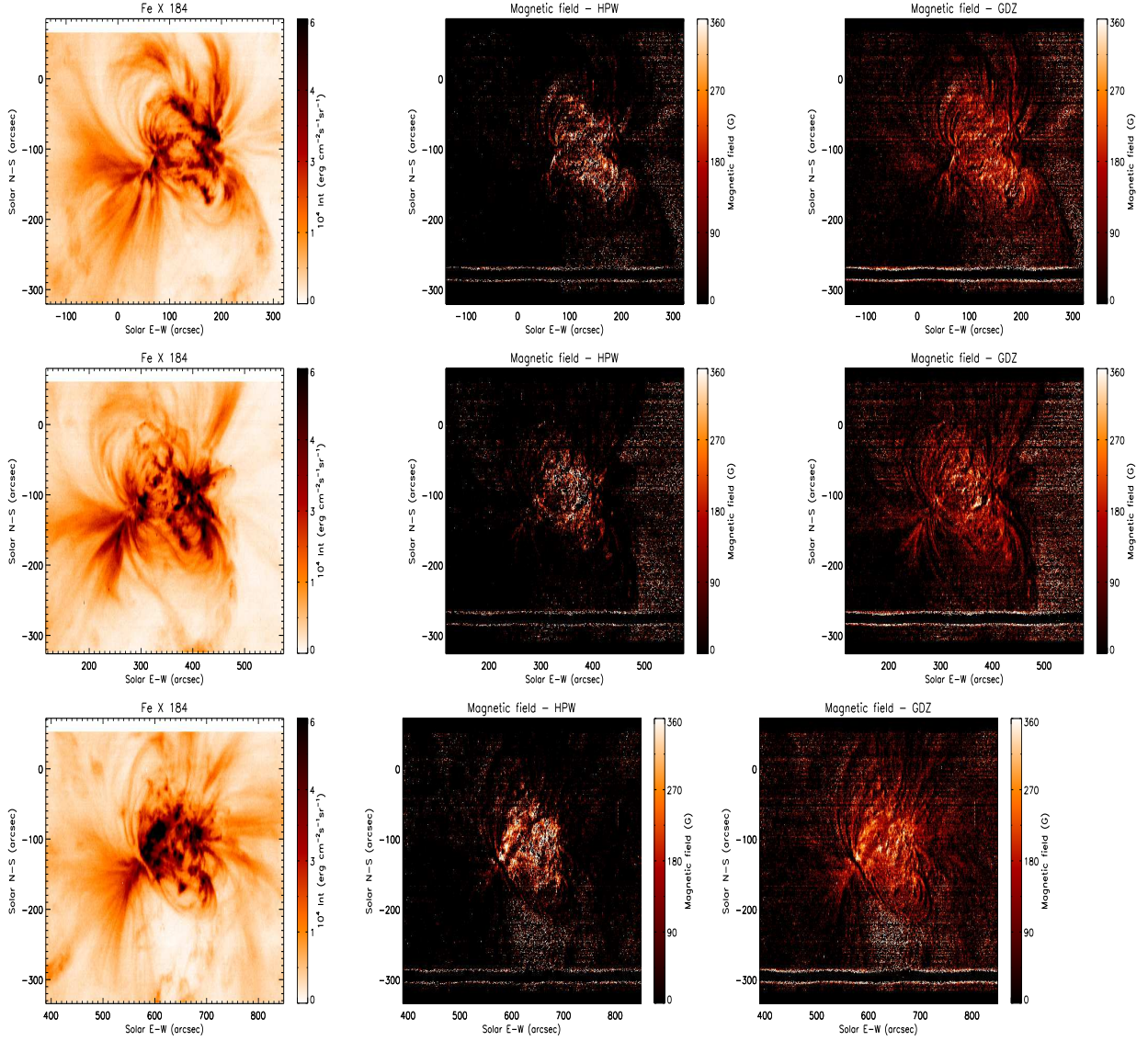


Fig. 9.— Comparison of magnetic field diagnostic results obtained with the HPW calibration (middle panels) and the GDZ calibration (right panels) from observations of AR10978.

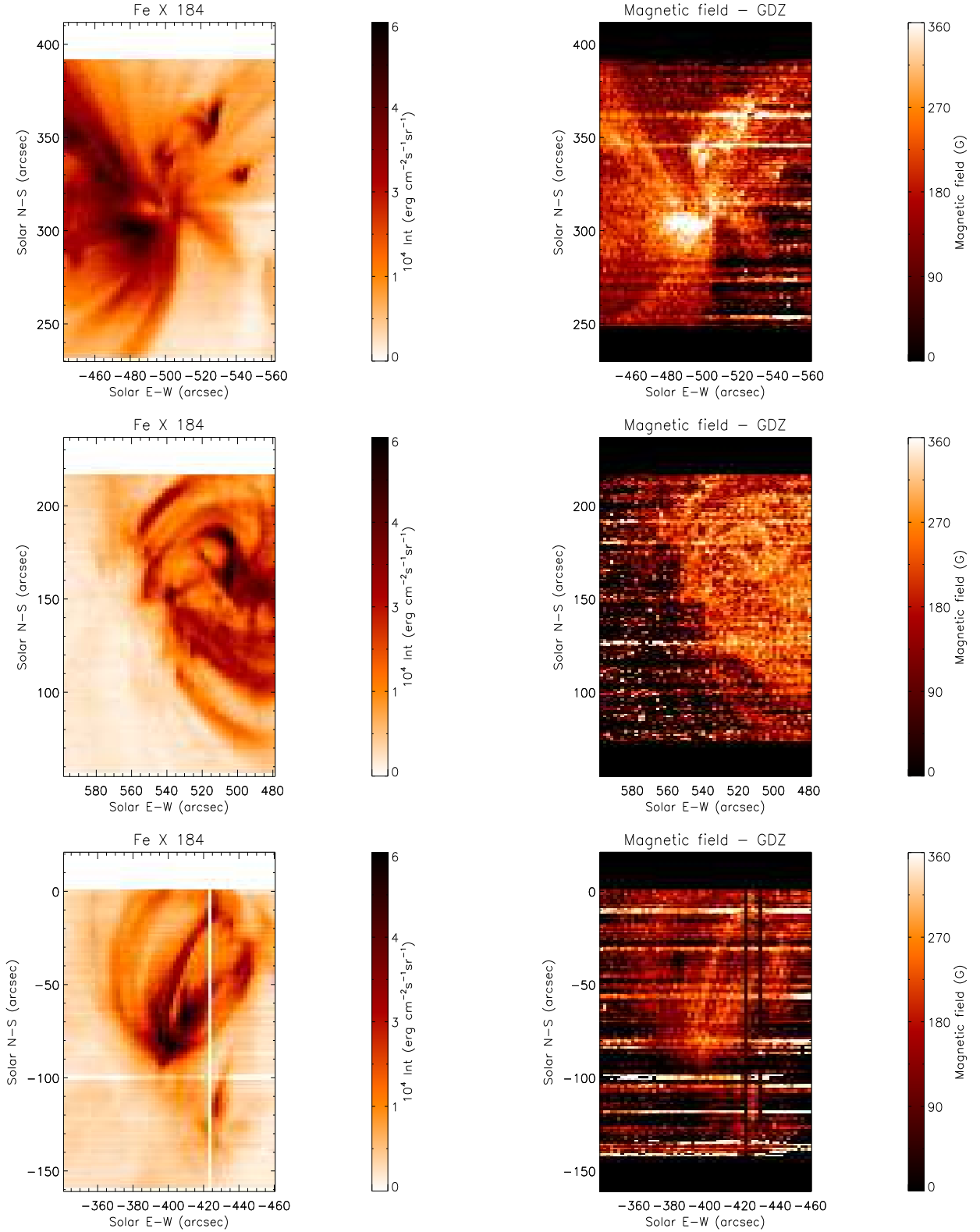


Fig. 10.— Effects of the degradation of the EIS sensitivity. Left panels: Fe X 184.53 Å intensity map; right panels: magnetic field measurements. **Top:** Active region observations taken on 16 March 2014 on AR12005; **Middle:** active region observations taken on 25 October 2016 on AR12603, **Bottom:** Active region observations taken on 28 December 2018 on an non-numbered AR

Magnetic field – HPW

